

Developing the tracking algorithm for Geant4 based simulated muon data, a step towards muography studies

Submitted By

Abhishek

School of Physical Sciences

National Institute of Science, Education and Research (NISER), Bhubaneswar



Under the Guidance of

Supervisor: Prof. Bedangadas Mohanty

School of Physical Sciences

National Institute of Science, Education and Research (NISER), Bhubaneswar

&

Co-supervisor: Dr. Raveendrababu Karnam

Center for Medical and Radiation Physics

National Institute of Science, Education and Research (NISER), Bhubaneswar

Acknowledgement

I would like to express my gratitude to my supervisor Prof. Bedangadas Mohanty for offering me the opportunity and consistent guidance throughout this project. I am also grateful to Dr. Raveendrababu Karnam for his consistent support and assistance. Lastly, I express my thanks to Dr. Varchaswi K S Kashyap for addressing my inquiries related to the project.

Abhishek

5th Year Integrated M.Sc.

School of Physical Sciences

NISER, Bhubaneswar

Abstract

This report presents the GEANT4 simulation studies of exploiting the cosmic-ray muons to image special nuclear materials like Uranium and the construction and characterization of the glass Resistive Plate Chambers (RPC) for the portable muon imaging telescope, which will be used for societal applications.

In the previous semester, the Point of Closest Approach (POCA) algorithm was used to reconstruct the image of a Lead block. The medium and high Z ($Z = \text{atomic number}$) materials were able to be distinguished using the muon scattering angle distributions. In this semester, the image reconstruction is improved using the Binned Clustering Algorithm (BCA) to image different Z materials simultaneously.

In the previous semester, a Resistance Plate Chamber (RPC) of size $200 \times 200 \times 2 \text{ mm}^3$ was built and a Printed Circuit Board (PCB) based read-out panel was developed. A comprehensive characterization studies are conducted on this RPC, including the measurement of efficiency, charge collection, and time resolution for various gas compositions. Another RPC of size $200 \times 200 \times 2 \text{ mm}^3$ and a PCB-based read-out panel is developed for the muon telescope.

Contents

	Page
Acknowledgement	i
Abstract	ii
1 Summary of the 9th semester project	2
1.1 Muography	2
1.1.1 Muon scattering tomography	2
1.2 GEANT4 simulation and POCA algorithm	2
2 Simulations: Improvement in the imaging algorithm	4
2.1 Acceptance of the muon telescope	4
2.2 Improvements in the imaging algorithm	5
2.2.1 Scattering angle cut	5
2.2.2 Voxelization of the 3D space	6
2.3 Binned Clustering Algorithm (BCA)	7
2.3.1 Parametrizing the accuracy of the BCA algorithm	8
2.3.2 Input Parameters for BCA algorithm	9
2.4 Imaging Spent Nuclear Fuel Dry Cask with BCA	9
3 Characterization of Resistive Plate Chamber (RPC)	11
3.1 RPC gas mixture	11
3.2 IV Characteristics of glass RPC	12
3.3 Muon Telescope: Trigger Criteria	13
3.4 RPC Efficiency Studies	14
3.4.1 RPC signal	14
3.4.2 RPC efficiency as a function of SF ₆ concentration	14
3.5 Charge collection as a function of SF ₆ concentration	15
3.6 Time resolution of RPC	16
3.7 Relative humidity test on acrylic chamber	18
3.8 Building the RPC and signal read-out panel	19

3.9	Future Directions	20
A		21
A.1	Point of Closet Approach	21
B.2	Procedure used to build the RPC	22
C.3	Procedure used to develop RPC signal read-out panel	22
D.4	RPC: Avalanche and Streamer	22
D.4.1	Avalanche Mode	23
D.4.2	Streamer Mode	23

Chapter 1

Summary of the 9th semester project

1.1 Muography

Cosmic rays are high-energy particles originating from various astrophysical sources [1]. These particles enter the Earth's upper atmosphere and collide with the atmospheric nuclei, producing hadrons like Pions and Kaons. The dominant decay modes of these hadrons produce naturally abundant muons at sea level. When muons pass through a given material, they lose their energy due to inelastic collisions with atomic electrons and deflect from their incident direction due to elastic scattering from nuclei. Muons have very high penetration capabilities since they are least likely to interact with the matter. Muography is an imaging technique that relies on the interaction of cosmic-ray muons with the object of interest.

1.1.1 Muon scattering tomography

Muon Scattering Tomography (MST) relies on the elastic multiple coulomb scattering of muons within a target material. As a muon traverses matter, it scatters multiple times, causing the outgoing angle to differ from the incoming angle. Charged particles typically follow a Rutherford scattering distribution [2], but the difference in angles, $\Delta\theta (\theta_{out} - \theta_{in})$, approximates a Gaussian distribution due to multiple scatterings.

$$\sigma(\theta) = \frac{z \cdot 13.6 \text{ MeV}}{p\beta c} \sqrt{\frac{x}{X_0}} \left[1 + 0.038 \cdot \ln \left(\frac{x}{X_0} \right) \right] \quad (1.1) \quad X_0 = \left[\frac{A \cdot 716.4 \text{ g cm}^{-2}}{Z(Z+1) \ln(287/\sqrt{Z})} \right] \left[\frac{1}{\rho} \right] \quad (1.2)$$

The standard deviation of the distribution, shown in Equation 1.1, is determined by the muon's momentum (p) and velocity (βc), its charge ($z = 1$), and the target's thickness (x) and radiation length (X_0). The radiation length is the mean distance over which an electron loses all $1/e$ of its energy as given in Equation 1.2. Due to its $\rho \cdot Z^2$ dependence, Muon scattering tomography is sensitive to dense, high atomic number objects. It is used in nuclear safety, security, and transport controls to detect illicit or hazardous materials. Here, ρ , A and Z represent the material's density, atomic mass, and atomic number.

1.2 GEANT4 simulation and POCA algorithm

- Muon telescope simulated with GEANT4 [3] see Figure 1.1. Cosmic ray muons generated with EcoMug [4]. Studied the spatial resolution as a function of distance

between the set of detectors. Differentiated materials using cosmic muon scattering tomography. The materials studied included Lead, Uranium, Iron, and Aluminium cubic blocks.

- The Point of Closest Approach (POCA) algorithm, detailed in appendix (A.1), finds the shortest distance between two non-intersecting tracks as shown in Appendix Figure A.1 in 3D space. The implementation in C was sourced from [5]
- Obtained a POCA image of a $100 \times 100 \times 100$ mm 3 Lead block.

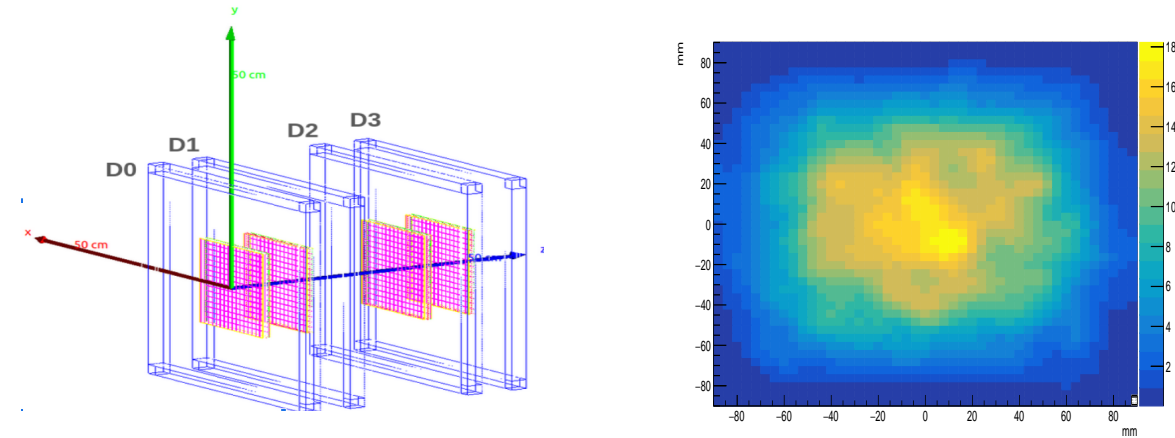


Fig. 1.1: Muoscope geometry developed in

GEANT4 [3]. D1 and D2 are referred to as inner detectors.

Fig. 1.2: A $100 \times 100 \times 100$ mm 3 Lead block 2D image is reconstructed using POCA.

- Developed a 200×200 mm 3 Resistive Plate Chamber (RPC) and a Printed Circuit Board (PCB) copper strips readout panel. A detailed procedure is given in appendix B.2 and C.3.

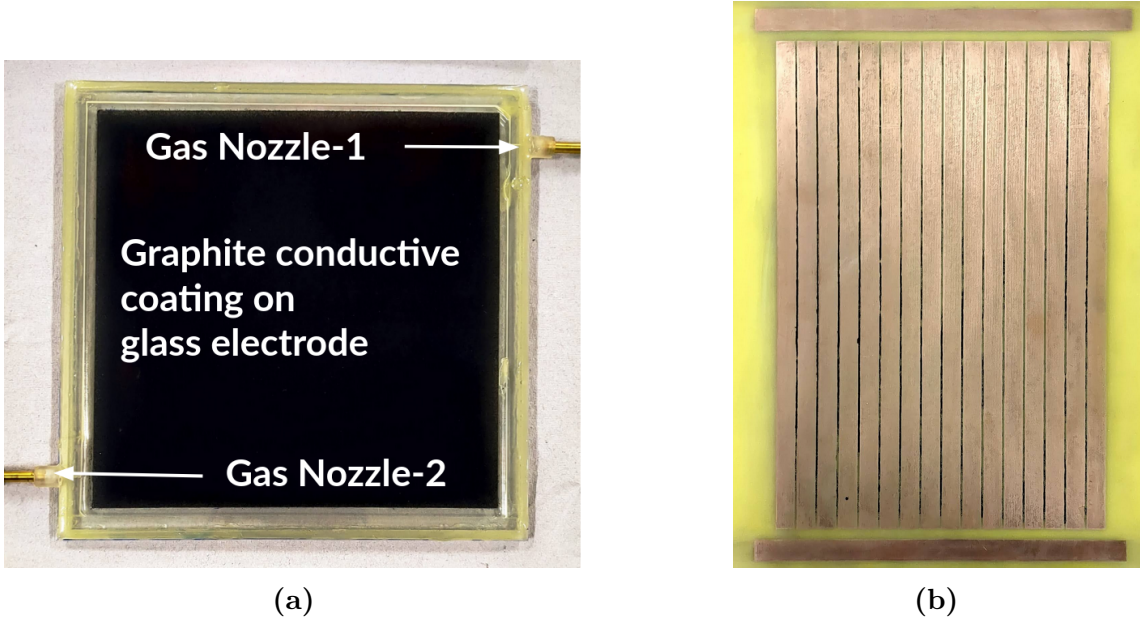


Fig. 1.3: (a) A glass RPC of size 200×200 mm 3 . (b) A PCB based copper strips readout panel.

Figure 1.3 shows the developed glass RPC and a copper strips readout panel for reading the signals from RPC.

Chapter 2

Simulations: Improvement in the imaging algorithm

Acceptance of the muon tracks on the telescope is studied as a function of the distance between the inner detectors of the telescope as shown in Figure 1.1. The Point of closest approach (POCA) algorithm was used in the last semester to image the Lead block of dimensions $100 \times 100 \times 100 \text{ mm}^3$ and was able to differentiate medium and high Z materials using the muon scattering angles in the materials. The POCA algorithm was not efficient in resolving the edges correctly and imaging multiple materials simultaneously. Improvements have been made to the image reconstruction algorithm to address these two issues.

2.1 Acceptance of the muon telescope

The acceptance of the muon telescope is defined as the fraction of muons that pass through the telescope. It is calculated using the following formula:

$$\text{Acceptance} = \frac{\text{Number of muons passing through all four layers}}{\text{Total number of muons generated}}. \quad (2.1)$$

The angular resolution of the muon telescope is defined as the minimum angle that the telescope can resolve. It is calculated using the following formula:

$$\text{Angular Resolution } (\sigma) = \frac{\Delta x \text{ (strip width)}}{\text{Distance between the detectors (W)}} \quad (2.2)$$

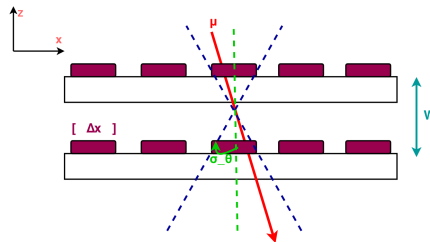


Fig. 2.1: Schematic to show the calculation of angular resolution (σ) [6] as a function of strip width and the distance between the detectors (D1 and D2) as shown in Figure 1.1.

Distance (w)(mm)	Acceptance(%)	Angular Resolution σ (rad)
200	12.38	0.045
250	10.22	0.036
300	8.37	0.030
350	6.90	0.026
400	5.73	0.022
450	5.19	0.020
500	4.52	0.018
550	3.9	0.016
600	3.6	0.015

Table 2.1: Acceptance and angular resolution of muon telescope as a function of the distance between the D1 and D2 as shown in Figure 1.1.

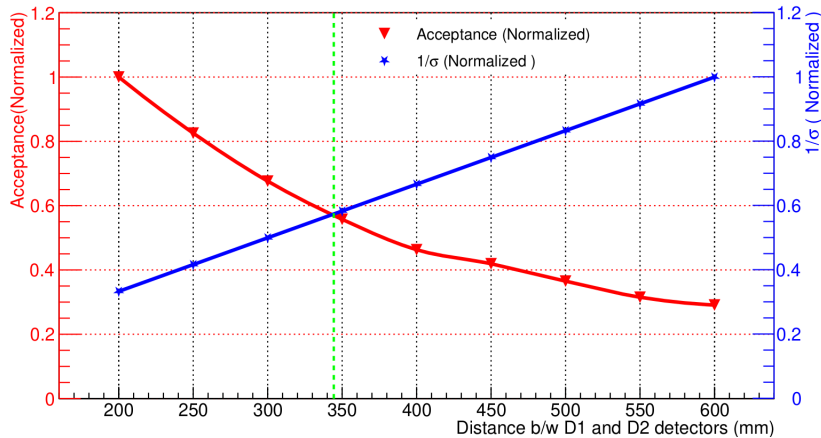


Fig. 2.2: Acceptance of the muon telescope on the red axis and inverse of the angular resolution on the blue axis.

In Figure 2.2, the acceptance of the muon telescope and angular resolution are plotted as a function of the distance between the inner detectors. The best trade-off has been made between the acceptance and the angular resolution at an **optimum distance = 34.5 mm** between the inner detectors as shown in Figure 1.1.

2.2 Improvements in the imaging algorithm

POCA is a simple algorithm that approximates the scattering point inside the material. The algorithm is based on the assumption that the muon scatters only once inside the material. It finds the mutual closest approach point of the muon incoming and outgoing tracks. But the presence of detector materials, like glass, acrylic, etc., gives false scattering points. To account for this issue, the following steps are implemented to improve the reconstruction algorithm:

2.2.1 Scattering angle cut

- The algorithm is modified to consider the only specific range of scattering angle ($\Delta\theta$) i.e $\Delta\theta_{min} < \Delta\theta < \Delta\theta_{max}$. This range is chosen because the low-momentum muons are

more likely to scatter multiple times and effectively have a larger scattering angle. On the other hand, larger momentum muons are less likely to scatter multiple times and have a smaller scattering angle. The following are the possible outcomes of the scattering angle:

1. If the scattering angle is small: (a) the point of interaction is a low-dense material or (b) muon has high momentum.
 2. If the scattering angle is large: (a) the point of interaction is a highly dense material or (b) muon has low momentum.
- To find the contribution of low-momentum muons in the scattering angle, a simulation is run without acrylic boxes and with acrylic boxes.

The scattering angle distribution without and with acrylic boxes, respectively, is shown in Figure 2.3. The scattering angle distribution with acrylic boxes is more spread out, indicating the contribution of low-momentum muons in the scattering angle. For imaging the target a cut on the scattering angle is applied, which is obtained from the GEANT4 simulation. Only those POCA points are considered which have scattering angles less than θ_{\max} cut given according to Figure 2.3a. In addition, the muon telescope has an **acceptance of $\approx 7\%$** , in which a low zenith angle having low momentum [7] muon tracks are accepted. Which leads to the larger spread of scattering angle distribution.

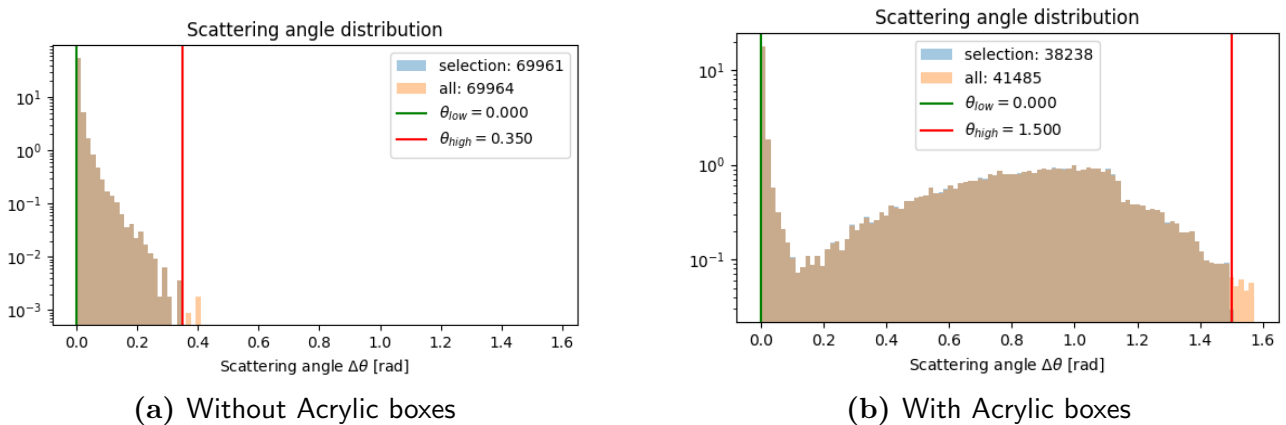


Fig. 2.3: Comparison of scattering angle distribution without and with acrylic boxes.

2.2.2 Voxelization of the 3D space

- The 3D space between the inner detectors as shown in Figure 1.1; is divided into small cubes (1000 mm^3) called voxels as shown in Figure 2.4.
- The POCA (x,y,z) points and corresponding scattering angles are stored in each voxel.
- Weight of each voxel is calculated using the POCA points and scattering angles according to Equation 2.5.

There are various methods to calculate the weight of each voxel i.e., the mean of POCA points, RMS of scattering angles, etc. However, in this study **Binned Clustering Algorithm** is used to compute the weight of each voxel.

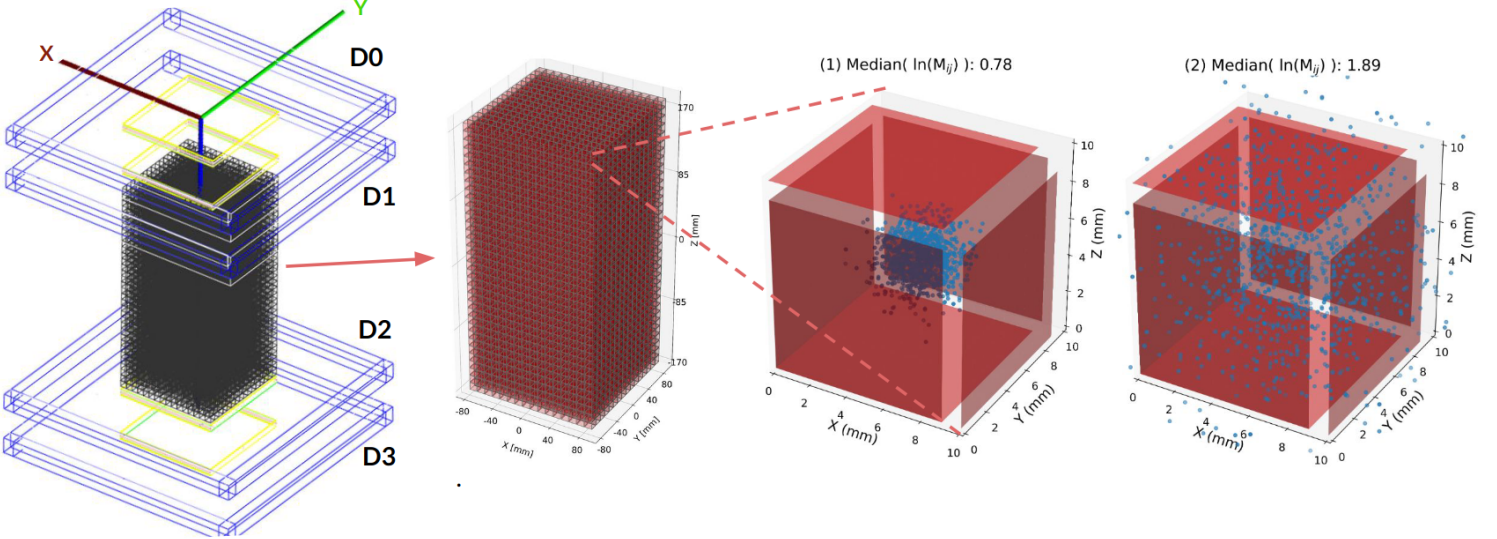


Fig. 2.4: Demonstration of voxelization and BCA.

2.3 Binned Clustering Algorithm (BCA)

The Binned Clustering Algorithm (BCA) [8] is a method to calculate the weight of each voxel. The decision-making algorithm identifies the spatial clustering of muons that pass through high-Z target material. It breaks down the volume of interest into cubic voxels, sized to detect the intended targets. For the target of a Lead block with dimensions $100 \times 100 \times 100 \text{ mm}^3$, a Volume of Interest (VOI) of $160 \times 160 \times 340 \text{ mm}^3$ is chosen. The algorithm then computes a ‘weighted clusteredness’ value for each voxel.

For every pair of muon tracks with scatter vertices¹ $v_i(x_i, y_i, z_i), v_j (x_j, y_j, z_j)$ located within the same voxel, the algorithm calculates a metric distance m_{ij} as shown in Equation 2.3.

$$m_{ij} = \|v_i - v_j\|. \quad (2.3)$$

This metric distance is then weighted by dividing it by the product of the scattering angles of the muons:

$$\tilde{m}_{ij} = \frac{m_{ij}}{\theta_i \cdot \theta_j} \quad (2.4)$$

where θ_i is the scatter angle of muon i . The median of these logarithmic values of the metric is then computed and used as the voxel’s final score.

$$\text{Score} = \text{Median}(\ln(\tilde{m}_{ij})) \quad (2.5)$$

This score is used to assign weight to each voxel, and plotting these voxels gives a reconstructed image of the target. The algorithm clusters POCA points in the region of interest based on their proximity, resulting in denser clusters for high-Z materials and, thus, smaller metric distances. It also factors in the muon scattering angle, with larger angles indicating high-Z materials and further reducing the score value (see Equation 2.5), and a lower score indicates high-Z material.

¹These vertices are scattering points computed using POCA algorithm.

2.3.1 Parametrizing the accuracy of the BCA algorithm

For quantifying the accuracy of the BCA algorithm, A reference 2D histogram is created, which has bins of size 100 mm^2 . Which contains the lowest score value (of reconstructed image) of each voxel in histogram bins numbered from $x = 3$ to 13 and $y = 3$ to 13 . it mimics the $100 \times 100 \times 100 \text{ mm}^3$. The Lead block and the rest of the bins are filled with 1 (highest value). The difference between the reference histogram and the reconstructed histogram is calculated, which will be used as an error. The error is calculated using the following method:

```
# Assume true_hist and recon_hist are 2D arrays of size 16x16 representing the
# reference and reconstructed histograms respectively.
# Calculate the difference between the two histograms to get the error matrix.
error_matrix = (true_hist - recon_hist)^2
# Calculate the mean of the error matrix to get the final error.
final_error = np.mean(error_matrix).
```

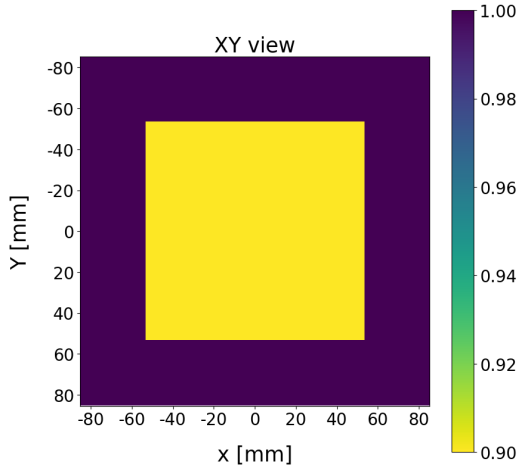


Fig. 2.5: True histogram of a 100 mm^3 Lead block.

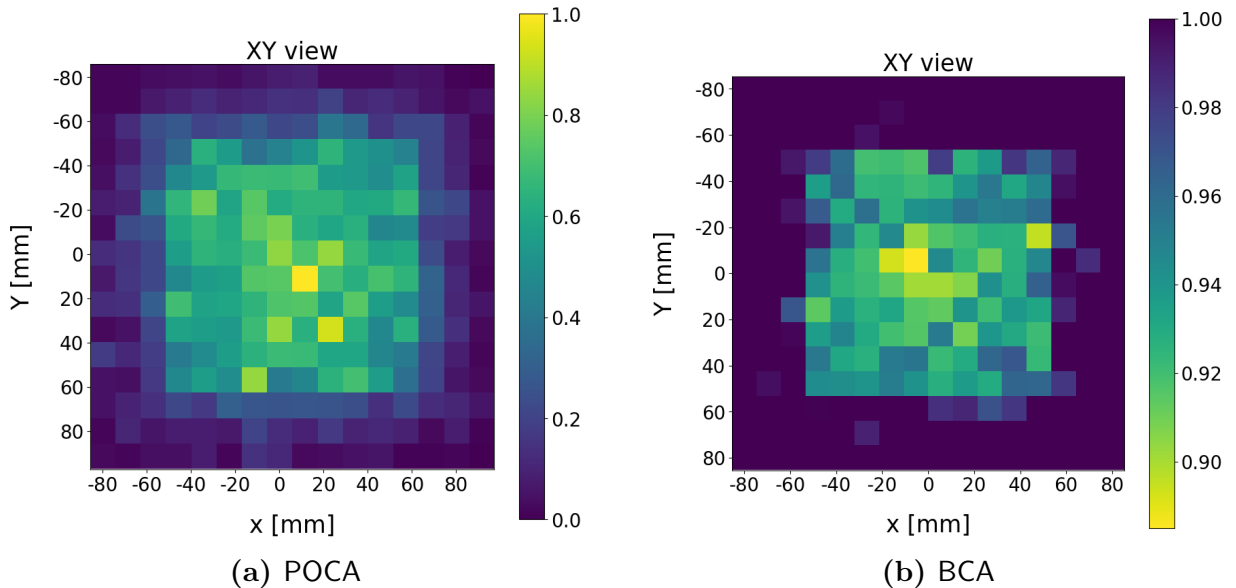


Fig. 2.6: (a) A $100 \times 100 \times 100 \text{ mm}^3$ Lead block histogram using POCA algorithm (Error = 0.122) and (b) histogram with Binned Clustering Algorithm (Error = 0.002).

NOTE: In Figure 2.6 It is important to note that the color bars for both histograms are not identical. In the case of POCA, the color bar represents the number of POCA points (normalized) in each bin. Conversely, for BCA, the color bar indicates the normalized score as shown in Equation 2.5.

2.3.2 Input Parameters for BCA algorithm

The following are the input parameters for the BCA algorithm:

```
'n_max_per_vox:int' - Maximum POCAs in voxel metric computation.  
'n_min_per_vox:int' - Minimum POCAs in voxel metric computation.  
'dtheta_range:Tuple[float]' - Scattering angle cut in radian.  
'voxel_size:float' - Size of the voxel in mm.  
'volume of interest:Tuple[float]' - Volume of interest in mm.
```

In output, the algorithm returns a 2D histogram of the volume of interest with the score value of each voxel.

2.4 Imaging Spent Nuclear Fuel Dry Cask with BCA

Spent nuclear fuel (SNF) is leftover radioactive material from nuclear reactors [9]. While it can't be used in reactors anymore, some of its parts could be used for weapons. It is stored in water pools near reactors, but that's not ideal. It's safer to move it to dry storage containers or special facilities. Since we don't have a permanent way to get rid of it yet, we might have to store it for longer than planned. Making sure none of this material goes missing or gets replaced with something else during storage is important. We need ways to check without opening the containers because that's costly and difficult. There Muon Scattering Tomography (MST) could be employed to image the SNF dry cask. The BCA algorithm is used to reconstruct the image of the SNF dry cask.

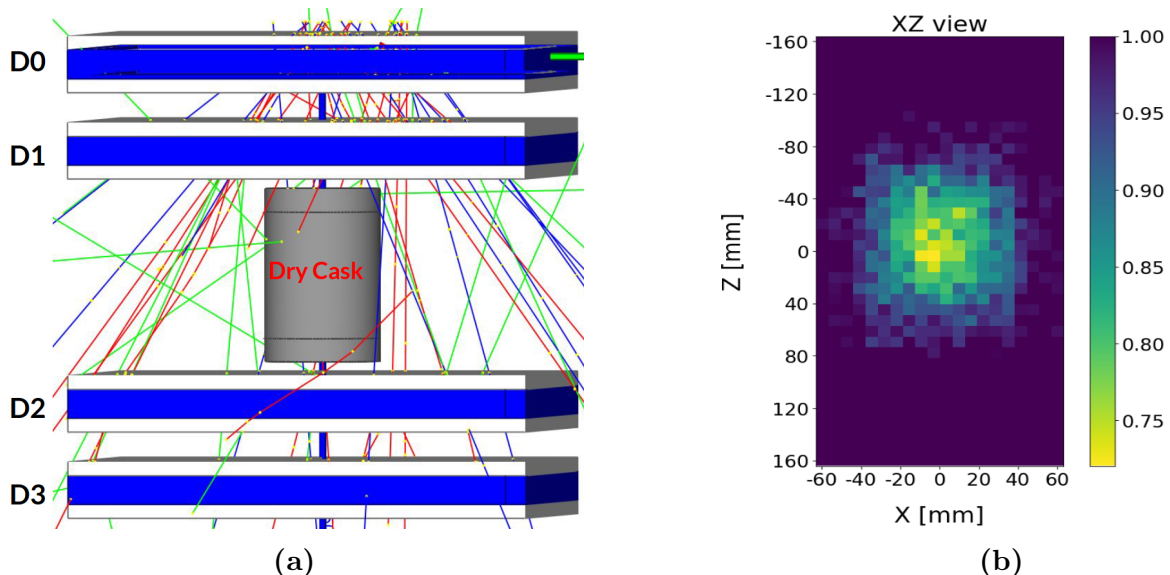


Fig. 2.7: (a) A dry Cask is placed in between detectors. (b) Shows a 2D image, an XZ projection, reconstructed using BCA.

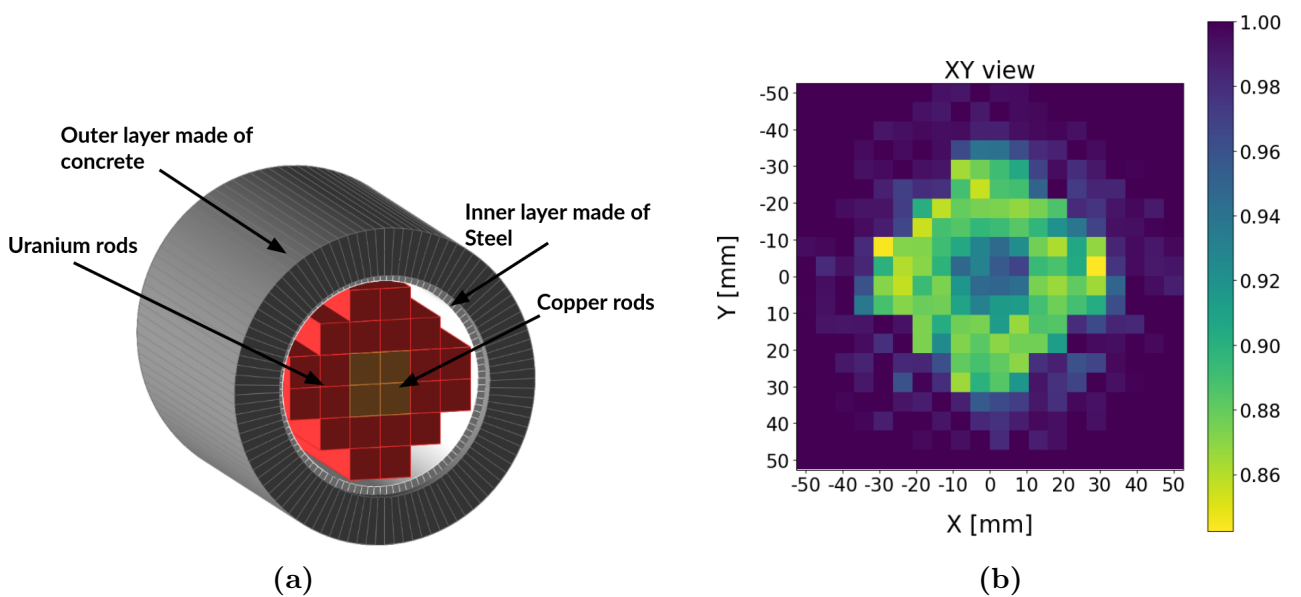


Fig. 2.8: (a) A dry cask made of concrete and steel containing Uranium (SNF) and copper rods is simulated in GEANT4. (b) presents the XY projection using the BCA reconstruction.

Component	Dimensions	Density(g/cm^3)
Concrete Shell	Outer radius: 10 cm, Inner radius: 70 mm, Height: 110 mm	2.4
Steel Container	Outer radius: 7 cm, Inner radius: 65 mm, Height: 100 mm	7.8
Uranium Rods	20 rods, Each rod: $10 \times 10 \times 100 \text{ mm}^3$	19.1
Copper Rods	4 rods, Each rod: $10 \times 10 \times 100 \text{ mm}^3$	8.9

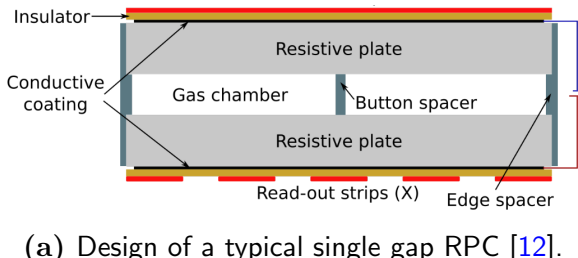
Table 2.2: Description of the Dry Cask components considered from the reference [10].

In Figure 2.8, the 2D image of the dry cask is reconstructed using the BCA algorithm. The XY projection of the dry cask is shown in Figure 2.8b and the XZ projection is shown in Figure 2.7b. Missing uranium rods are visible in the XY projection. Copper rods and Uranium rods are differentiated in the reconstructed image. Therefore, the BCA algorithm is efficient in differentiating medium and high-Z materials.

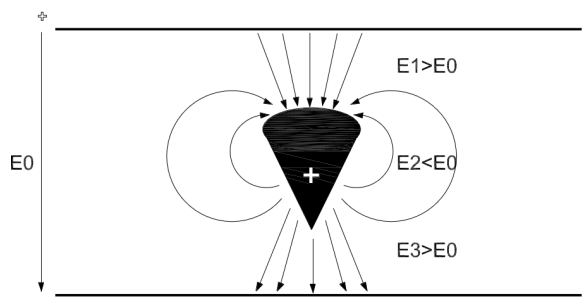
Chapter 3

Characterization of Resistive Plate Chamber (RPC)

In the last semester, a $200 \times 200 \times 2 \text{ mm}^3$ Resistive Plate Chamber (RPC) was developed using graphite-coated glass electrodes. Please see the appendix B.2 for a detailed procedure. The RPC [11] is a gaseous detector used in high-energy physics experiments to detect charged particles. The RPCs are made up of two parallel resistive plates with a gas gap in between. When a charged particle passes through the gas gap, it ionizes the gas molecules, and the resulting electrons drift toward the anode and cathode plates. The electrons are accelerated in the electric field and produce an avalanche of electrons. The avalanche of electrons will induce a signal on the readout strips that could be read by the electronics. Since RPCs are easy to construct, have a fast response time, and better spatial resolution. RPC electrodes are highly resistive, making charge localized and providing accurate position information. It makes RPCs suitable for muon tomography studies. More details about the working principle of RPC are discussed in Appendix D.4.



(a) Design of a typical single gap RPC [12].



(b) Avalanche formation inside the gas gap. [13]

Fig. 3.1: (a) A typical single gap RPC design. (b) This represents the schematic of an avalanche and the resulting electric field variations within the RPC. E_0 is the uniform field applied across the electrodes, while E_1 , E_2 , and E_3 denote the effective fields at the avalanche charge distribution's tip, center, and tail, respectively.

3.1 RPC gas mixture

Gaseous detectors in proportional mode require sufficient primary ionization by the incident particle or radiation for a large signal via charge multiplication. Noble gases with lower ionization potential are commonly used. However, interaction with gas molecules can lead to photon

emission, causing spurious avalanches and loss of proportionality and position resolution. To mitigate this, quench gases that absorb ultraviolet photons are used. Small amounts of highly electronegative gases are added to prevent streamer development and stabilize operations. The choice of gases and their proportions significantly affect detector characteristics. This study uses the following gas mixture:

- **R-134A ($C_2H_2F_4$):** A freon variant with a large primary ionization cross-section and slight electronegativity, used for avalanche control.
- **Iso-butane ($i-C_4H_{10}$):** A quencher absorbing photon energy kept below flammability limit due to combustibility.
- **Sulphur hexafluoride (SF_6):** A strongly electronegative gas reducing streamer formation through electron attachment.

The gas mixture used consists of 95.3% R-134A, 4.5% $i-C_4H_{10}$, and 0.2% SF_6 , as per the proportions mentioned in reference [12]. Furthermore, studies have been conducted to determine the optimal gas proportions for muography. In these studies, the concentrations of R-134A and SF_6 were varied while keeping the concentration of $i-C_4H_{10}$ constant. The objective is to identify the optimal operating voltage and gas mixture proportion that results in minimal charge collection and maximizes efficiency.

Following are the RPC responses that are calculated:

- **IV Characteristics:** The current-voltage (IV) characteristic curve is a plot of the current flowing through the RPC as a function of the applied voltage. The IV curve is used to determine the knee point and resistances of the RPC gas gap.
- **Efficiency:** The efficiency of the RPC is defined as the fraction of muons that pass through the RPC and produce a signal.
- **Charge collection:** RPC charge is the total charge induced on the readout strips.
- **Time resolution:** The time resolution of the RPC is defined as the time difference between the arrival of the muon at the RPC and the trigger signal.

3.2 IV Characteristics of glass RPC

A 2 mm gas gap glass RPC ($160 \times 160 \text{ mm}^2$). High voltage is applied across the graphite coating on the glass plates as shown in Figure 3.3d. After varying the voltage applied from 1 kV to 12 kV, the flow of the current is recorded.

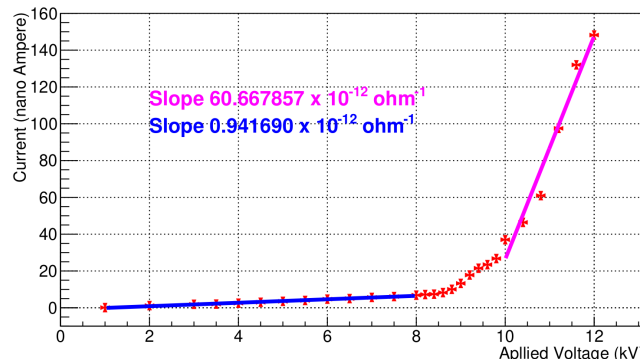
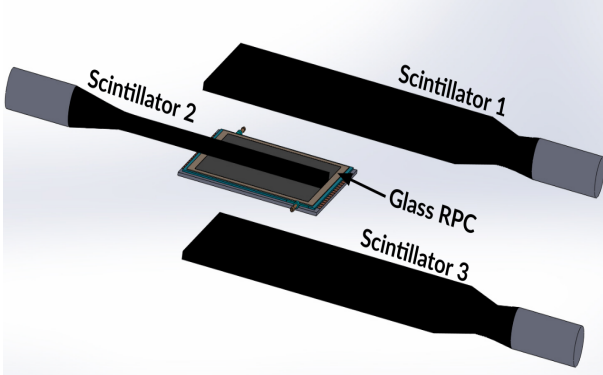


Fig. 3.2: IV Characteristics of a glass RPC.

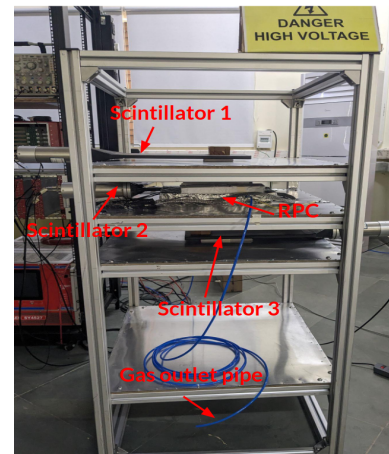
Figure 3.2 presents the IV characteristics of a glass RPC. 28 data points are recorded in two hours. Initially, the gas acts as an insulator, preventing current flow, with the only contribution coming from the acrylic spacer. As the voltage increases, the gas begins to ionize, allowing current to flow. The slope of the curve represents the reciprocal of the gas gap's resistance. This behavior is by Ohm's law, expressed as $V = IR$, where V is the voltage, I is the current, and R is the resistance. The resistance before the gas starts to conduct is given by 1.062×10^{12} ohms, and after the gas starts to conduct; it becomes 1.65×10^{10} ohms.

3.3 Muon Telescope: Trigger Criteria

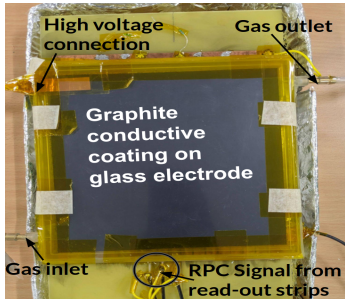
A muon telescope is built using three plastic scintillator detectors. This telescope sets up coincidence criteria for cosmic muon pulses from the glass RPC.



(a)



(b)



(c)



(d)

Fig. 3.3: (a)The muon telescope schematic comprises plastic scintillators, with Scintillators 1 and 3 of dimensions $400 \times 200 \times 10 \text{ mm}^3$, while Scintillator 2 dimensions $300 \times 40 \times 10 \text{ mm}^3$. (b) A muon telescope is used for measuring the efficiency of the glass RPC. (c) A $200 \times 200 \text{ mm}^2$ glass RPC (d) CAEN SY4527 power supply system is used for providing high voltage to the RPC.

How it measures the efficiency of the RPC is explained below:

- Muons are identified by their ability to pass through the telescope's three layers of scintillators. If a charged particle is detected in all three layers, it's identified as a muon.
- The trigger pulse, represented by the coincidence of scintillator 1, scintillator 2, and scintillator 3, is referred to as the three-fold signal (3F).

- A signal detected in the RPC in coincidence with the 3F signal is classified as a four-fold signal (4F). The coincidence is stretched to 100 ns to ensure passage of muon.
- The efficiency of the RPC is calculated as the ratio of the number of 4F signals to the number of 3F signals.

3.4 RPC Efficiency Studies

As explained in previous sections, the efficiency of the RPC is defined as the ratio of the number of 4F signals to the number of 3F signals.

3.4.1 RPC signal

The RPC signal is the total charge induced [14] on the readout strips. An oscilloscope (Tektronix MDO3024) is used to record the pulse.

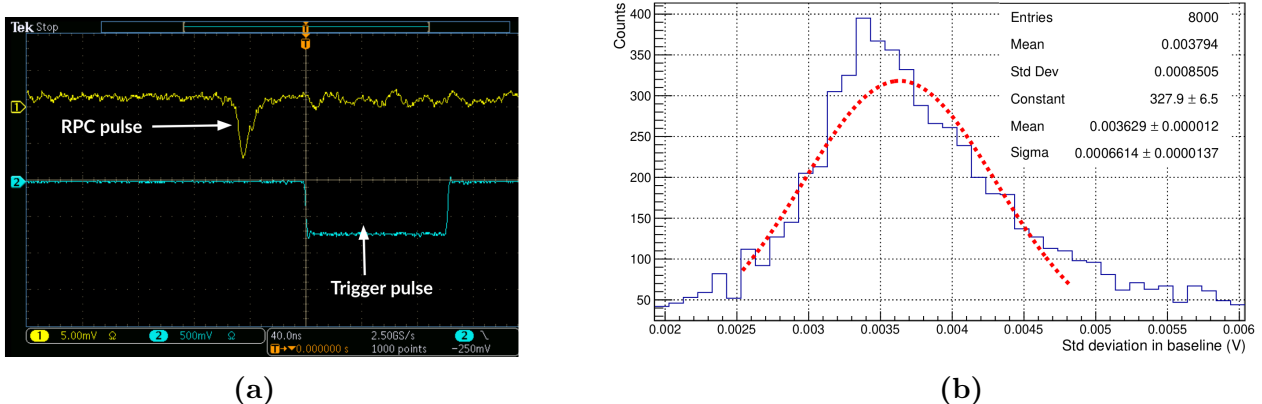


Fig. 3.4: (a) A RPC and trigger signal recorded by the oscilloscope. (b) The threshold for the RPC pulse is set at 5σ of the baseline noise.

Both RPC and trigger signals are captured from the oscilloscope for offline analysis. A threshold for the RPC pulse is established by calculating the baseline noise, which is the signal fluctuation before the RPC pulse arrival. Out of ten thousand sampled points for each signal, the initial 250 are considered the baseline. The baseline standard deviation for each pulse is computed to form a distribution 3.4b. The threshold for the RPC pulse is set at $5\sigma = 3.3 \text{ mV}$ of this distribution. If RPC pulse amplitude exceeds this threshold (3.3 mV); it is considered a signal. For calculating efficiency, the following formula is used:

$$\text{Efficiency}(\%) = (\text{Number of signals above threshold} / \text{Total number of signals}) \times 100 \quad (3.1)$$

3.4.2 RPC efficiency as a function of SF₆ concentration

In this study, a gas mixture (R134A:9.53, I-Butane:4.5, SF₆:0.2) at 10 SCCM is flushed into the RPC, with varying SF₆ concentrations to examine its impact on RPC efficiency and charge collection. For each gas mixture tabulated in Table 3.1, a scan of efficiency is recorded at 16 voltage values from 8 kV to 11 kV in steps of 200 V. At each voltage 1000 signals are collected along with the trigger which took 1 hour approximately. The aim is to minimize charge collection, as excessive collection can harm the electronics and increase the RPC's dead time. For muography, an RPC with an excellent spatial resolution (<9 mm) is required. However,

RPCs with high charge collection have been observed to distribute charge across the readout strips. A smaller spread, hence lower charge collection, is preferred for better spatial resolution. In avalanche mode, the spread is around 4 mm in radius [15], and in streamer mode, it's 12 mm [16]. To reduce charge collection, SF₆ is added in proportions as listed in Table 3.1.

	R134A (SCCM)	I-Butane (SCCM)	SF ₆ (SCCM)
Rate 1	9.55	0.45	0.00
Rate 2	9.53	0.45	0.02
Rate 3	9.50	0.45	0.05
Rate 4	9.47	0.45	0.08
Rate 5	9.53	0.45	0.10

Table 3.1: Flush rate of gases in Standard Cubic Centimeters per Minute (SCCM).

Roles of gases in the RPC gas mixture are discussed in section 3.1. The RPC efficiency is calculated for each gas mixture mentioned in Table 3.1. In Figure 3.5, efficiency is plotted as a function of the applied voltage for each gas mixture. The inclusion of SF₆ has been observed to notably decrease efficiency, and with an increase in SF₆ concentration.

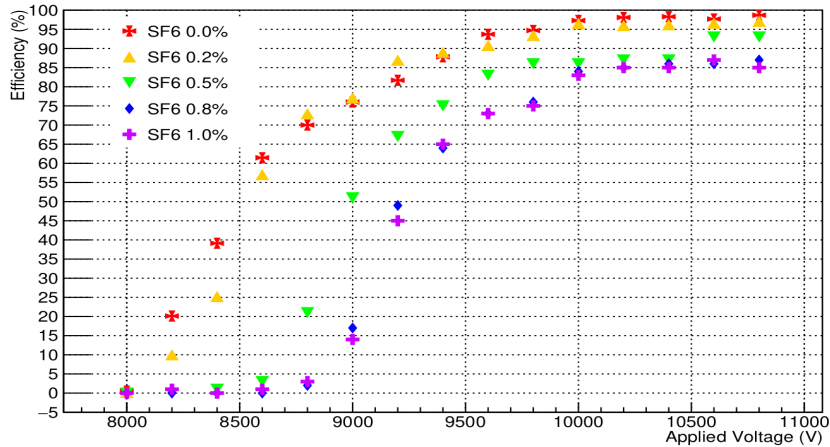


Fig. 3.5: RPC efficiency as a function of SF₆ concentration and applied voltage.

3.5 Charge collection as a function of SF₆ concentration

After the RPC signal is captured, the charge collection is analyzed by integrating the RPC pulse is shown in Figure 3.11a in the time window of -100 ns to +100 ns.

$$\text{Charge} = \frac{1}{\text{Amplification factor}} \int_{-100 \text{ ns}}^{+100 \text{ ns}} \frac{\text{Voltage}}{\text{Resistance}} dt \quad (3.2)$$

In Equation 3.2, the resistance refers to the impedance of electronics used for signal collection. The amplification factor is the RPC signal's amplification by the CAEN Mod N979 fast amplifier. The voltage represents the RPC signal's height in fig 3.11b. The integration is performed using Python's `scipy.integrate.trapezoid` library.

It is found from Figure 3.5 that if the applied voltage exceeds 10 kV, the RPC efficiency is above 85%. Hence, 10 kV is used as the operating voltage for charge collection studies.

Additionally, charge collection is also studied at 10.2 kV and 10.4 kV for all gas mixtures listed in table 3.1.

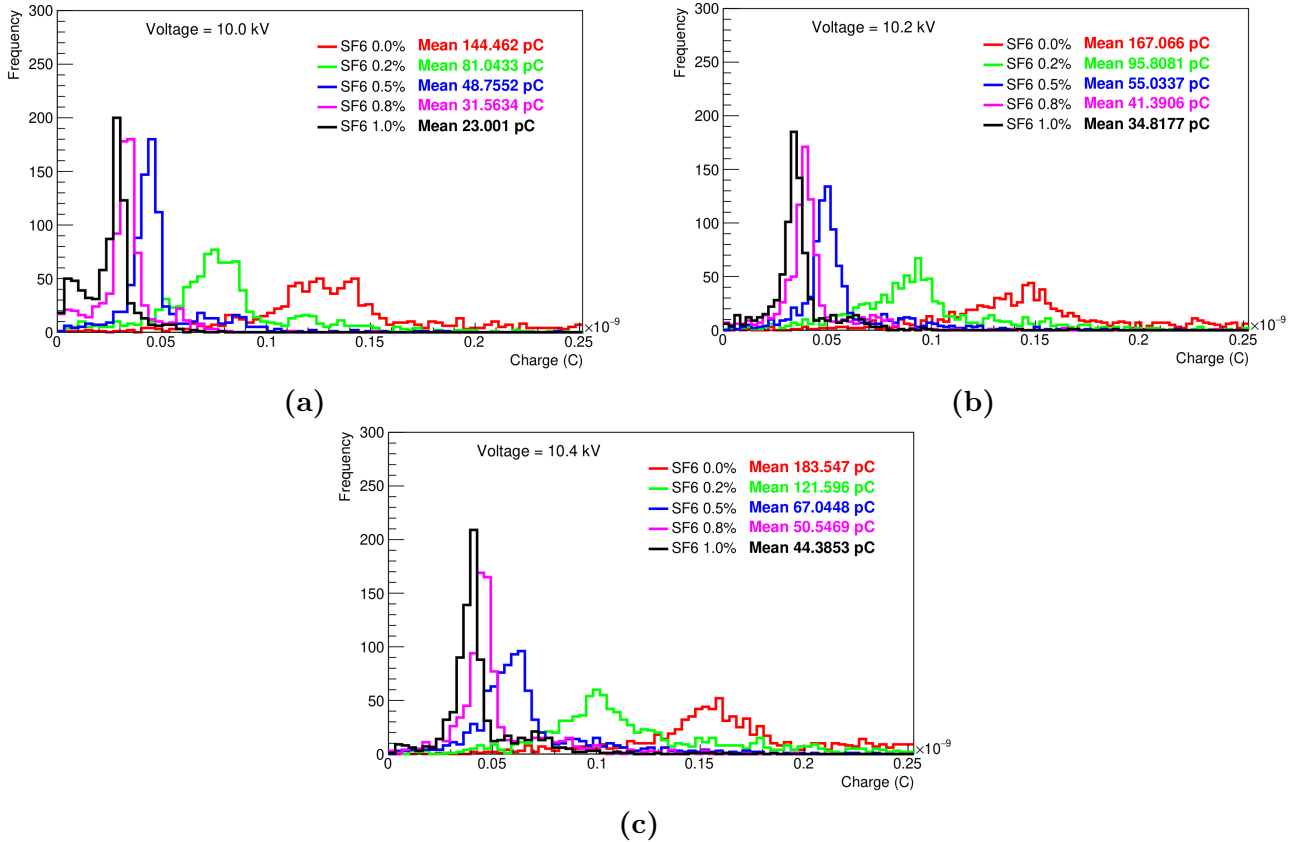


Fig. 3.6: Charge spectra at (a) 10.0 kV. (b) 10.2 kV. (c) 10.4 kV.

Figure 3.6 shows the charge spectra for each gas mixture plotted at 10.0 kV, 10.2 kV, and 10.4 kV. It is shown that the charge collection decreases with an increase in SF₆ concentration. The peaks shift to the left side, with an increase in SF₆ concentration. Table 3.2 shows the efficiency and charge collection for different SF₆ concentrations at 10 kV, 10.2 kV, and 10.4 kV. Both efficiency and charge collection decrease with an increase in SF₆ concentration.

3.6 Time resolution of RPC

The time resolution of the RPC is defined as the standard deviation of the time differences between the 10% height of the RPC pulse as shown in Figure 3.11b and the trigger pulse. Figure 3.7 shows the time resolution of the RPC as a function of the applied voltage 10 kV and SF₆ concentration 0.5%.

Voltage (kV)	SF_6 Concentration (%)	Efficiency (%)	Mean Charge (pC)
10	0.0	97.3	144.47
	0.2	96.5	81.04
	0.5	86.5	48.76
	0.8	84.6	31.60
	1.0	83.1	23.00
10.2	0.0	98.1	167.07
	0.2	96.0	95.81
	0.5	87.51	55.03
	0.8	85.68	41.40
	1.0	85.28	34.82
10.4	0.0	98.29	183.54
	0.2	96.2	121.60
	0.5	87.0	67.04
	0.8	86.0	50.55
	1.0	85.68	44.38

Table 3.2: Efficiency and charge collection of RPC as a function of SF_6 concentration.

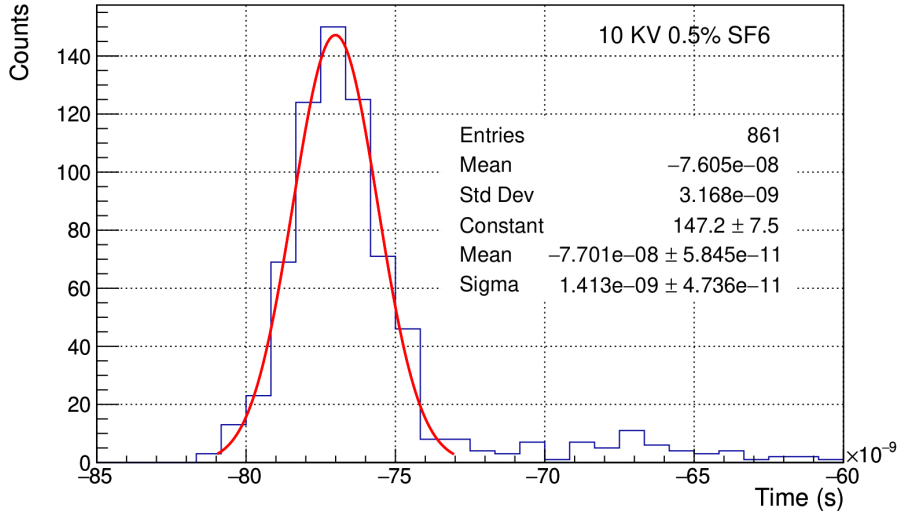


Fig. 3.7: Time resolution of RPC.

Table 3.3 shows the time resolution of the RPC for different SF_6 concentrations. It is observed that the time resolution increases with an increase in SF_6 concentration. Since SF_6 is a strongly electronegative gas, it arrests avalanche development through electron attachment, effectively reducing streamer formation. However, this also increases the time resolution of the RPC. Similar findings were also noted in Section 3.9.1 of the thesis [13]. Since the rate of cosmic muons ($100 \text{ Hz}/m^2$) [17] is quite low compared to collider experiments like CMS $7.5 \times 10^4 \text{ Hz}/m^2$ [18], therefore, time resolution in the order of nanosecond is good for muography studies.

SF_6 (%)	Time Resolution (ns)
0.0	1.27
0.2	1.41
0.5	1.42
0.8	1.56
1.0	1.69

Table 3.3: SF_6 concentration and time resolution.

3.7 Relative humidity test on acrylic chamber

The efficiency of RPC remains relatively stable with changes in Relative Humidity (RH) at room temperature. However, at higher temperatures, RH does impact efficiency, as noted in [19]. Given that RPCs might be operated outdoors for muography studies, an acrylic chamber has been designed to shield the RPC from external temperature and humidity fluctuations.

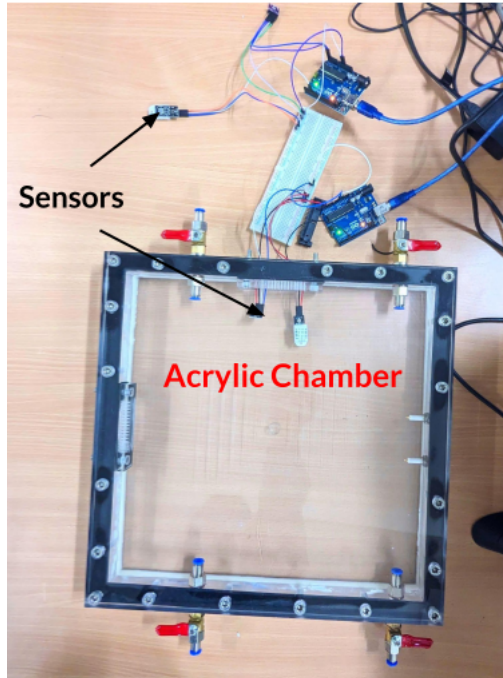


Fig. 3.8: Acrylic chamber for housing the RPC.

An acrylic chamber is used in GEANT4 simulation as shown in Figure 1.1 and is designed to house the RPC. The chamber shown in Figure 3.8 is designed to be gas-tight and has a gas inlet and outlet for flushing the RPC with the gas mixture. The chamber is tested for humidity stability and gas tightness. Two BMP280 sensors are used to measure the humidity and temperature inside and outside the chamber. Humidity data is collected using the Arduino Uno microcontroller for 30 days and plotted in Figure 3.9.

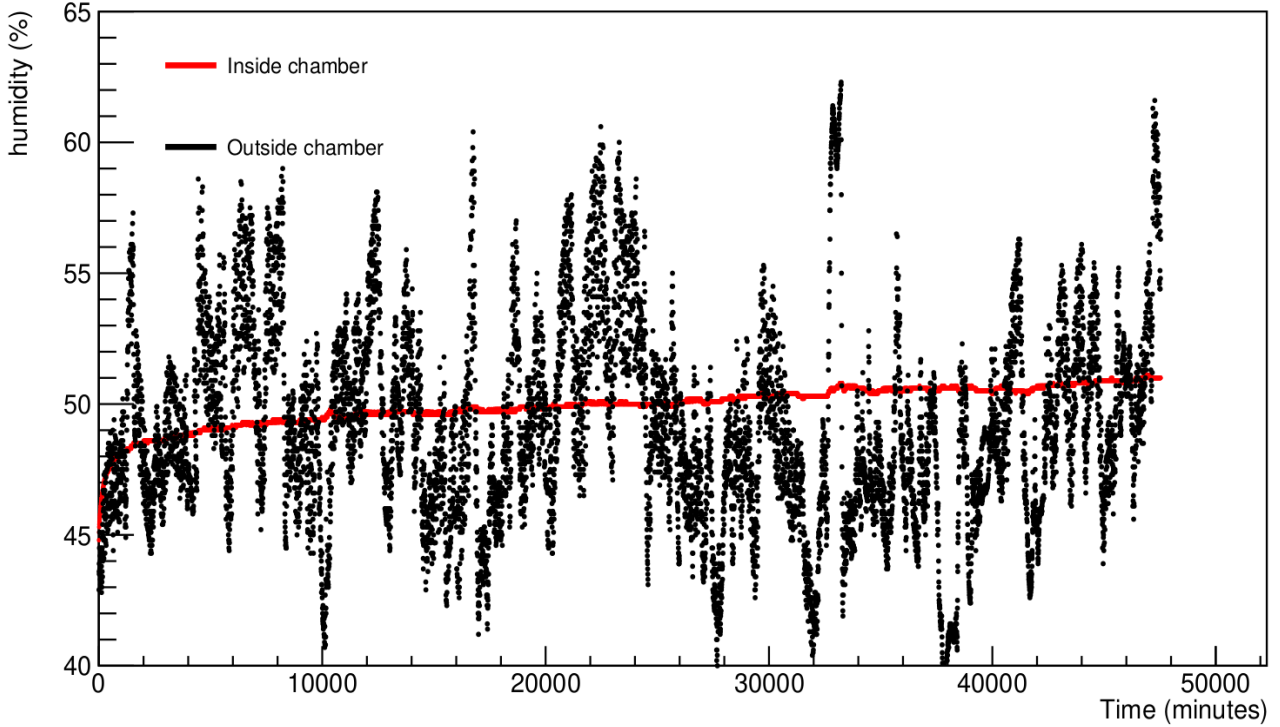


Fig. 3.9: Humidity levels are monitored both outside and inside the chamber for 30 days.

In Figure 3.9, the graph displays humidity levels over 15-minute intervals. Outside the chamber, humidity fluctuates significantly, while inside, it changes gradually before reaching a stable level. Therefore, this chamber could be used to place RPC.

3.8 Building the RPC and signal read-out panel

A glass RPC and copper strip readout was developed in the last semester. In this semester, one more RPC was developed of similar size ($200 \times 200 \times 3 \text{ mm}^3$) as the previous one. A printed circuit board (PCB) based on 16 strips of read-out panel is developed to read the RPC signals. The full procedure is given in Appendix B.2 and C.3. Following are the steps used to build an RPC:

- Glass plates cleaned and coated with graphite paint for electrodes. Please see Figure 3.10b for the surface resistance map.
- Electrodes separated by acrylic and edged with spacers, sealed with epoxy.
- Gas nozzles added, assembly left to dry for a week.

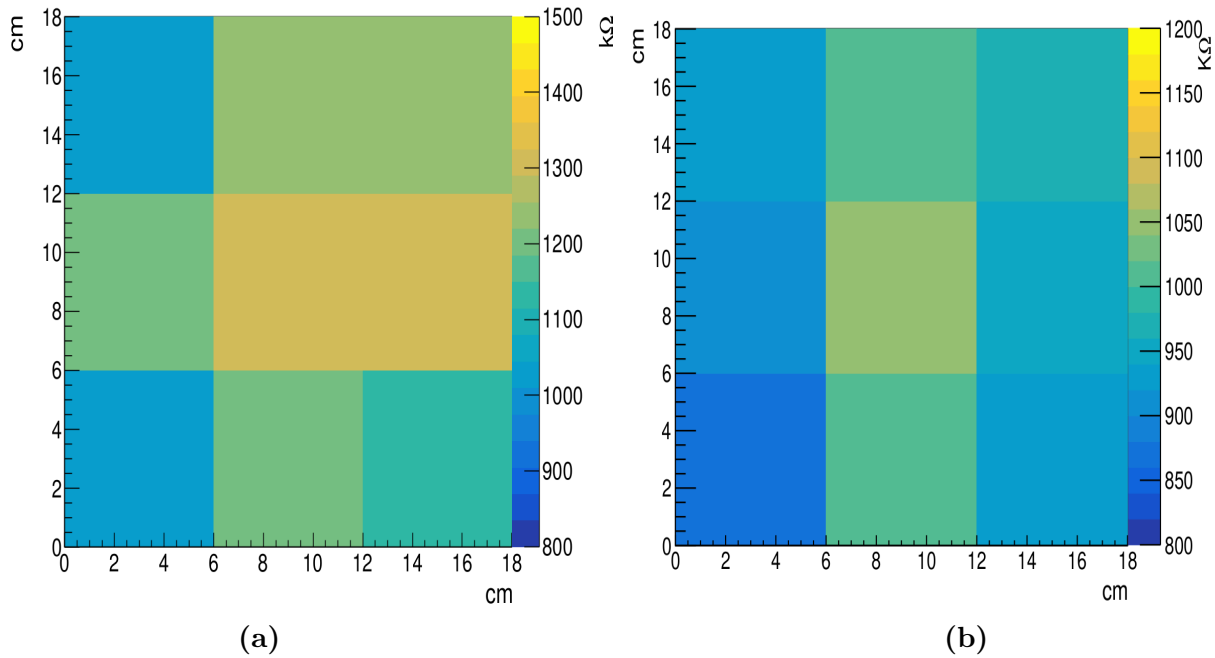


Fig. 3.10: Surface resistance map of graphite coated glass electrode (a) G5 and (b) G6.

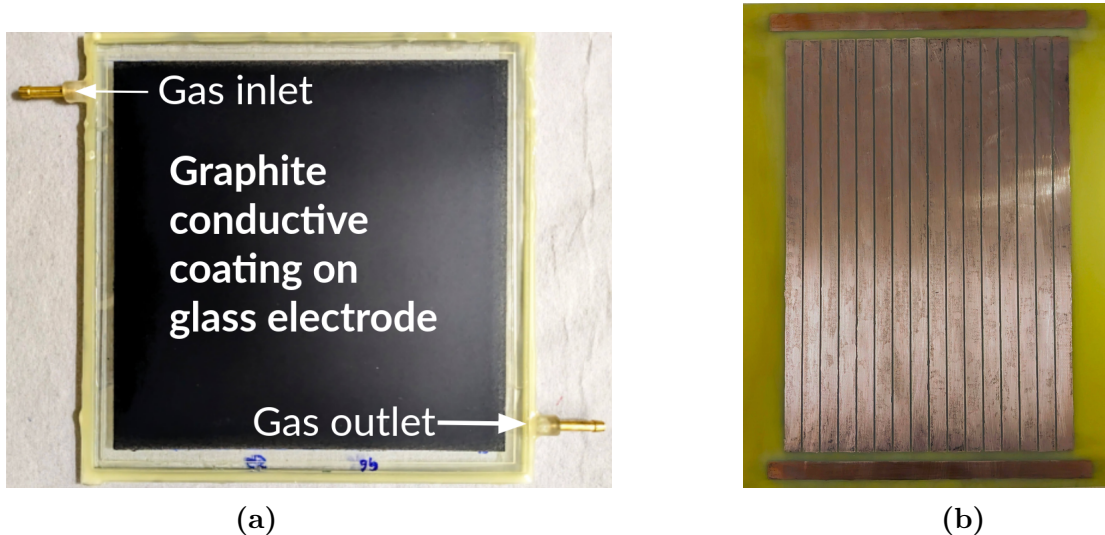


Fig. 3.11: (a) A $200 \times 200 \text{ mm}^2$ glass RPC (b) A Printed Circuit Board (PCB) panel is used to develop 16 strips of copper read-out for reading the RPC signal.

3.9 Future Directions

- A study has been conducted to regulate charge collection using SF_6 . The effects of Isobutane will be investigated [20].
 - Signal storage will be implemented using a Petiroc ASIC and FPGA-based data acquisition system.
 - Two glass RPCs have been built for developing the muon telescope. Two more RPCs will be developed.

Appendix A

A.1 Point of Closet Approach

- 1. The shortest line segment between two lines "a" and "b" can be found by minimizing the distance function $\|Pb - Pa\|^2$ and solving the resulting equations for μ_a and μ_b , then substituting these values into the line equations to obtain the intersection points [5].
- 2. The shortest distance between two lines is found along a line that stands at right angles to both of them. You can find this by first getting the direction vector for each line and then finding their cross-product, which gives you the direction of the shortest line. You can then calculate where this shortest line intersects one of the original lines. The coordinates at this intersection point will give you the closest point on that line.

The dot product equations for finding the shortest line segment between two lines are:

$$\begin{aligned}(Pa - Pb) \cdot (P2 - P1) &= 0 \\ (Pa - Pb) \cdot (P4 - P3) &= 0\end{aligned}$$

Expanding these equations with the line equations:

$$\begin{aligned}(P1 - P3 + \mu_a(P2 - P1) - \mu_b(P4 - P3)) \cdot (P2 - P1) &= 0 \\ (P1 - P3 + \mu_a(P2 - P1) - \mu_b(P4 - P3)) \cdot (P4 - P3) &= 0 \\ (P1 - P3) \cdot (P2 - P1) + \mu_a(P2 - P1) \cdot (P2 - P1) - \mu_b(P4 - P3) \cdot (P2 - P1) &= 0 \\ (P1 - P3) \cdot (P4 - P3) + \mu_a(P2 - P1) \cdot (P4 - P3) - \mu_b(P4 - P3) \cdot (P4 - P3) &= 0\end{aligned}$$

The equations for finding μ_a and μ_b , which determine the shortest line segment between two lines, are:

$$\begin{aligned}\mu_a &= (d_{1343} d_{4321} - d_{1321} d_{4343}) / (d_{2121} d_{4343} - d_{4321} d_{4321}) \\ \mu_b &= (d_{1343} + \mu_a * d_{4321}) / d_{4343}\end{aligned}$$

where $d_{mnop} = (x_m - x_n)(x_o - x_p) + (y_m - y_n)(y_o - y_p) + (z_m - z_n)(z_o - z_p)$.

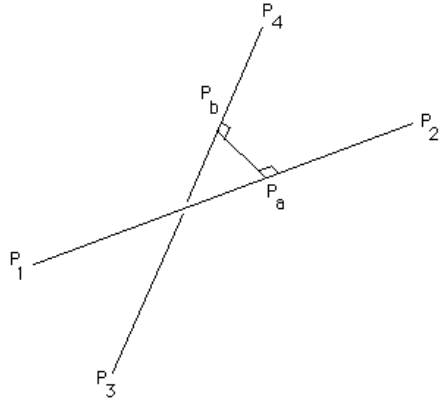


Fig. A.1: In 3D, the shortest distance between two tracks is from P_a to P_b , with the midpoint serving as the POCA point.

B.2 Procedure used to build the RPC

- Two glass plates with dimensions $200 \times 200 \times 3 \text{ mm}^3$ were thoroughly washed with lab clean soap and distilled water. Then, they are wiped with 2-propanol.
- These glass plates are coated with graphite paint using an INGCO 450 W paint spray gun. The surface resistance of the electrodes is measured using a locally made copper zig. The measured surface resistance values across the electrodes are about $1 \text{ M}\Omega/\square$.
- The electrodes are separated by placing a 2 mm thick and 10 mm diameter acrylic spacer at the center and $200 \text{ mm} \times 10 \text{ mm} \times 2 \text{ mm}$ spacers at the edges. Two gas nozzles are placed at the opposite corners of the RPC. Araldite standard epoxy adhesive is applied to the glass and spacers to isolate the RPC gap from the outer atmosphere. This assembly is left for a week for curing. The assembled RPC is shown in Figure 3.3d.

C.3 Procedure used to develop RPC signal read-out panel

A $300 \text{ mm} \times 300 \text{ mm} \times 1.5 \text{ mm}$ copper cladded PCB is etched with ferric chloride to develop copper strips. The copper strips are 9 mm in width and 230 mm in length.

- A design was printed with black ink on an A4 sheet. This sheet is placed on the PCB, and then the design is ironed on the PCB. The ink is diffused on the PCB.
- This PCB is placed inside the ferric chloride solution. The copper where ink is not deposited is etched out by the solution.

D.4 RPC: Avalanche and Streamer

The Resistive Plate Chamber (RPC) is a gaseous detector. Charged particles or radiation ionize gas molecules in the RPC chamber, with ions and electrons moving toward the cathode

and anode in an electric field. High enough fields cause secondary ionization. The total electron count is given by $n = n_0 e^{(\alpha - \beta)x}$, where n_0 is primary electrons, α is the first Townsend (β) is the attachment coefficient (number of electrons captured by the electronegative gas molecules per unit length).

D.4.1 Avalanche Mode

When particles with high energy traverse the gas within the detector, they initiate the creation of primary electrons and ions. As these primary particles move under the influence of the applied electric field, they lead to additional ionizations. This chain reaction of ionization events, referred to as an avalanche, results in the induction of a current on the read-out strips of the detector. In this region, known as the proportional region, the charge that is produced is in direct proportion to the number of primary particles, and this relationship is governed by the gas gain (G). For a low value of G, the charge that is generated is relatively small, necessitating amplification to produce signals that can be detected. The ability of the RPC to manage a rapid influx of particles is attributed to the small magnitude of the charge it produces. The area of a discharge cell, which is determined by the total charge deposited, plays a significant role in the rate of detection of the RPC. To operate in the avalanche mode, a mixture of gases, specifically $C_2H_2F_4$, i- C_4H_{10} , and SF_6 , is used. Among these, $C_2H_2F_4$ serves as the primary medium for ionization.

D.4.2 Streamer Mode

As the applied voltage increases, the gain (G) rises, and at a certain threshold, photons start contributing to avalanche development, causing avalanches to spread. When the total charge in the avalanche approaches the point where space charge effects become significant, a plasma channel forms between electrodes, leading to spark formation and discharge of a local area due to bulk resistivity. This phenomenon, known as the Raether limit [21], occurs at pressures close to or higher than 1 atm and depends on the RPC's design, gas mixture, and pressure. In streamer mode, where charge generation is larger (about 50 pC to a few nC), subsequent amplification is unnecessary. However, this mode has a longer dead time, restricting operation to low count rate conditions. A gas mixture of argon and $C_2H_2F_4$, with a small amount of i- C_4H_{10} as a quencher, is used to operate in streamer mode.

Bibliography

- [1] G. Bonomi, P. Checchia, M. D'Errico, D. Pagano, and G. Saracino. Applications of cosmic-ray muons. *Progress in Particle and Nuclear Physics*, 112:103768, 2020.
- [2] E. Rutherford. Lxxix. the scattering of α and β particles by matter and the structure of the atom. *The London, Edinburgh, and Dublin Philosophical Magazine and Journal of Science*, 21(125):669–688, 1911.
- [3] S. Agostinelli, J. Allison, K. Amako, J. Apostolakis, H. Araujo, P. Arce, M. Asai, D. Axen, S. Banerjee, G. Barrand, F. Behner, L. Bellagamba, J. Boudreau, L. Broglia, A. Brunengo, H. Burkhardt, S. Chauvie, J. Chuma, R. Chytracek, G. Cooperman, G. Cosmo, P. Degtyarenko, A. Dell'Acqua, G. Depaola, D. Dietrich, R. Enami, A. Feliciello, C. Ferguson, H. Fesefeldt, G. Folger, F. Foppiano, A. Forti, S. Garelli, S. Giani, R. Giannitrapani, D. Gibin, J.J. Gómez Cadenas, I. González, G. Gracia Abril, G. Greeniaus, W. Greiner, V. Grichine, A. Grossheim, S. Guatelli, P. Gumplinger, R. Hamatsu, K. Hashimoto, H. Hasui, A. Heikkinen, A. Howard, V. Ivanchenko, A. Johnson, F.W. Jones, J. Kallenbach, N. Kanaya, M. Kawabata, Y. Kawabata, M. Kawaguti, S. Kelner, P. Kent, A. Kimura, T. Kodama, R. Kokoulin, M. Kossov, H. Kurashige, E. Lamanna, T. Lampén, V. Lara, V. Lefebure, F. Lei, M. Liendl, W. Lockman, F. Longo, S. Magni, M. Maire, E. Medernach, K. Minamimoto, P. Mora de Freitas, Y. Morita, K. Murakami, M. Nagamatu, R. Nartallo, P. Nieminen, T. Nishimura, K. Ohtsubo, M. Okamura, S. O'Neale, Y. Oohata, K. Paech, J. Perl, A. Pfeiffer, M.G. Pia, F. Ranjard, A. Rybin, S. Sadilov, E. Di Salvo, G. Santin, T. Sasaki, N. Savvas, Y. Sawada, S. Scherer, S. Sei, V. Sirotenko, D. Smith, N. Starkov, H. Stoecker, J. Sulkimo, M. Takahata, S. Tanaka, E. Tcherniaev, E. Safai Tehrani, M. Tropeano, P. Truscott, H. Uno, L. Urban, P. Urban, M. Verderi, A. Walkden, W. Wander, H. Weber, J.P. Wellisch, T. Wenaus, D.C. Williams, D. Wright, T. Yamada, H. Yoshida, and D. Zschiesche. Geant4—a simulation toolkit. *Nuclear Instruments and Methods in Physics Research Section A: Accelerators, Spectrometers, Detectors and Associated Equipment*, 506(3):250–303, 2003.
- [4] D Pagano, G Bonomi, A Donzella, A Zenoni, G Zumerle, and N Zurlo. EcoMug: An efficient COsmic MUon generator for cosmic-ray muon applications. *Nucl. Instrum. Methods Phys. Res. A*, 1014(165732):165732, October 2021.
- [5] Paul Bourke. Geometry in computer graphics - point, line, plane, October 1988. Accessed: November 14th, 2023.
- [6] Sophie Wuyckens. Development of a compact telescope for cosmic muon flux and density measurements. Master's thesis, Centre for Cosmology, Particle Physics and Phenomenology, Université Catholique de Louvain, Belgium., 2022.
- [7] P. Achard, O. Adriani, M. Aguilar-Benitez, M. van den Akker, J. Alcaraz, G. Alemani, J. Allaby, A. Aloisio, M.G. Alviggi, H. Anderhub, V.P. Andreev, F. Anselmo, A. Arefiev,

T. Azemoon, T. Aziz, P. Bagnaia, A. Bajo, G. Baksay, L. Baksay, J. Bähr, S.V. Baldew, S. Banerjee, Sw. Banerjee, A. Barczyk, R. Barillère, P. Bartalini, M. Basile, N. Batalova, R. Battiston, A. Bay, F. Becattini, U. Becker, F. Behner, L. Bellucci, R. Berbeco, J. Berdugo, P. Berges, B. Bertucci, B.L. Betev, M. Biasini, M. Biglietti, A. Biland, J.J. Blaising, S.C. Blyth, G.J. Bobbink, A. Böhm, L. Boldizsar, B. Borgia, S. Bottai, D. Bourilkov, M. Bourquin, S. Braccini, J.G. Branson, F. Brochu, J.D. Burger, W.J. Burger, X.D. Cai, M. Capell, G. Cara Romeo, G. Carlino, A. Cartacci, J. Casaus, F. Cavallari, N. Cavallo, C. Cecchi, M. Cerrada, M. Chamizo, T. Chiarusi, Y.H. Chang, M. Chemarin, A. Chen, G. Chen, G.M. Chen, H.F. Chen, H.S. Chen, G. Chiefari, L. Cifarelli, F. Cindolo, I. Clare, R. Clare, G. Coignet, N. Colino, S. Costantini, B. de la Cruz, S. Cucciarelli, J.A. van Dalen, R. de Asmundis, P. Déglon, J. Debreczeni, A. Degré, K. Dehmelt, K. Deiters, D. della Volpe, E. Delmeire, P. Denes, F. DeNotaristefani, A. De Salvo, M. Diemoz, M. Dierckxsens, L.K. Ding, C. Dionisi, M. Dittmar, A. Doria, M.T. Dova, D. Duchesneau, M. Duda, I. Duran, B. Echenard, A. Eline, A. El Hage, H. El Mamouni, A. Engler, F.J. Eppling, P. Extermann, G. Faber, M.A. Falagan, S. Falciano, A. Favara, J. Fay, O. Fedin, M. Felcini, T. Ferguson, H. Fesefeldt, E. Fiandrini, J.H. Field, F. Filthaut, W. Fisher, I. Fisk, G. Forconi, K. Freudenreich, C. Furetta, Yu. Galaktionov, S.N. Ganguli, P. Garcia-Abia, M. Gataullin, S. Gentile, S. Giagu, Z.F. Gong, H.J. Grabosch, G. Grenier, O. Grimm, H. Groenstege, M.W. Gruenewald, M. Guida, Y.N. Guo, S. Gupta, V.K. Gupta, A. Gurtu, L.J. Gutay, D. Haas, Ch. Haller, D. Hatzifotiadou, Y. Hayashi, Z.X. He, T. Hebbeker, A. Hervé, J. Hirschfelder, H. Hofer, H. Hofer, M. Hohlmann, G. Holzner, S.R. Hou, A.X. Huo, Y. Hu, N. Ito, B.N. Jin, C.L. Jing, L.W. Jones, P. de Jong, I. Josa-Mutuberría, V. Kantserov, M. Kaur, S. Kawakami, M.N. Kienzle-Focacci, J.K. Kim, J. Kirkby, W. Kittel, A. Klimentov, A.C. König, E. Kok, A. Korn, M. Kopal, V. Koutsenko, M. Kräber, H.H. Kuang, R.W. Kraemer, A. Krüger, J. Kuijpers, A. Kunin, P. Ladron de Guevara, I. Laktineh, G. Landi, M. Lebeau, A. Lebedev, P. Lebrun, P. Lecomte, P. Lecoq, P. Le Coultre, J.M. Le Goff, Y. Lei, H. Leich, R. Leiste, M. Levchenko, P. Levchenko, C. Li, L. Li, Z.C. Li, S. Likhoded, C.H. Lin, W.T. Lin, F.L. Linde, L. Lista, Z.A. Liu, W. Lohmann, E. Longo, Y.S. Lu, C. Luci, L. Luminari, W. Lustermann, W.G. Ma, X.H. Ma, Y.Q. Ma, L. Malgeri, A. Malinin, C. Maña, J. Mans, J.P. Martin, F. Marzano, K. Mazumdar, R.R. McNeil, S. Mele, X.W. Meng, L. Merola, M. Meschini, W.J. Metzger, A. Mihul, A. van Mil, H. Milcent, G. Mirabelli, J. Mnich, G.B. Mohanty, B. Monteleoni, G.S. Muanza, A.J.M. Muijs, B. Musicar, M. Musy, S. Nagy, R. Nahnhauer, V.A. Naumov, S. Natale, M. Napolitano, F. Nessi-Tedaldi, H. Newman, A. Nisati, T. Novak, H. Nowak, R. Ofierzynski, G. Organtini, I. Pal, C. Palomares, P. Paolucci, R. Paramatti, J.-F. Parriaud, G. Passaleva, S. Patricelli, T. Paul, M. Pauluzzi, C. Paus, F. Pauss, M. Pedace, S. Pensotti, D. Perret-Gallix, B. Petersen, D. Piccolo, F. Pierella, M. Pieri, M. Pioppi, P.A. Piroué, E. Pistoletti, V. Plyaskin, M. Pohl, V. Pojidaev, J. Pothier, D. Prokofiev, J. Quartieri, C.R. Qing, G. Rahal-Callot, M.A. Rahaman, P. Raics, N. Raja, R. Ramelli, P.G. Rancoita, R. Ranieri, A. Raspereza, K.C. Ravindran, P. Razis, D. Ren, M. Rescigno, S. Reucroft, P. Rewiersma, S. Riemann, K. Riles, B.P. Roe, A. Rojkov, L. Romero, A. Rosca, C. Rosemann, C. Rosenbleck, S. Rosier-Lees, S. Roth, J.A. Rubio, G. Ruggiero, H. Rykaczewski, R. Saidi, A. Sakharov, S. Saremi, S. Sarkar, J. Salicio, E. Sanchez, C. Schäfer, V. Schegelsky, V. Schmitt, B. Schoeneich, H. Schopper, D.J. Schotanus, C. Sciacca, L. Servoli, C.Q. Shen, S. Shevchenko, N. Shivarov, V. Shoutko, E. Shumilov, A. Shvorob, D. Son, C. Souga, P. Spillantini, M. Steuer, D.P. Stickland, B. Stoyanov, A. Straessner, K. Sudhakar, H. Sulanke, G. Sultanov, L.Z. Sun, S. Sushkov, H. Suter, J.D. Swain, Z. Szillasi, X.W. Tang, P. Tarjan, L. Tauscher, L. Taylor, B. Tellili, D. Teyssier, C. Timmermans, Samuel C.C. Ting, S.M. Ting, S.C. Tonwar, J. Tóth,

- G. Trowitzsch, C. Tully, K.L. Tung, J. Ulbricht, M. Unger, E. Valente, H. Verkooijen, R.T. van de Walle, R. Vasquez, V. Vespremi, G. Vesztregombi, I. Veltlitsky, D. Vicinanza, G. Viertel, S. Villa, M. Vivargent, S. Vlachos, I. Vodopianov, H. Vogel, H. Vogt, I. Vorobiev, A.A. Vorobyov, M. Wadhwa, R.G. Wang, Q. Wang, X.L. Wang, X.W. Wang, Z.M. Wang, M. Weber, R. van Wijk, T.A.M. Wijnen, H. Wilkens, S. Wynhoff, L. Xia, Y.P. Xu, J.S. Xu, Z.Z. Xu, J. Yamamoto, B.Z. Yang, C.G. Yang, H.J. Yang, M. Yang, X.F. Yang, Z.G. Yao, S.C. Yeh, Z.Q. Yu, An. Zalite, Yu. Zalite, C. Zhang, F. Zhang, J. Zhang, S. Zhang, Z.P. Zhang, J. Zhao, S.J. Zhou, G.Y. Zhu, R.Y. Zhu, H.L. Zhuang, Q.Q. Zhu, A. Zichichi, B. Zimmermann, M. Zöller, and A.N.M. Zwart. Measurement of the atmospheric muon spectrum from 20 to 3000 gev. *Physics Letters B*, 598(1):15–32, 2004.
- [8] C Thomay, J J Velthuis, P Baesso, D Cussans, P A W Morris, C Steer, J Burns, S Quillin, and M Stapleton. A binned clustering algorithm to detect high-z material using cosmic ray muons. *Journal of Instrumentation*, 8(10):P10013, oct 2013.
 - [9] Zhengzhi Liu. Methodologies for imaging a used nuclear fuel dry storage cask with cosmic ray muon computed tomography. 2018.
 - [10] The Southern States Energy Board (SSEB). Dry cask storage of nuclear spent fuel. Online.
 - [11] R. Santonico and R. Cardarelli. Development of resistive plate counters. *Nuclear Instruments and Methods in Physics Research*, 187(2):377–380, 1981.
 - [12] Abhik Jash. *Studies on the physics of Resistive Plate Chambers in relation to the INO experiment*. PhD thesis, Calcutta, VECC, 2018.
 - [13] Satyanarayana Bheesette. *Design and Characterisation Studies of Resistive Plate Chambers*. PhD thesis, Indian Inst. Tech., Mumbai, 2009.
 - [14] Christian Lippmann and Werner Riegler. Detailed rpc avalanche simulations. *Nuclear Instruments and Methods in Physics Research Section A: Accelerators, Spectrometers, Detectors and Associated Equipment*, 533(1):11–15, 2004. Proceedings of the Seventh International Workshop on Resistive Plate Chambers and Related Detectors.
 - [15] S. Narita, Y. Hoshi, K. Neichi, and A. Yamaguchi. Induced charge profile in a glass rpc operated in avalanche mode. *IEEE Transactions on Nuclear Science*, 60(6):4656–4659, 2013.
 - [16] S. Narita, M. Shoji, Y. Hoshi, D. Miura, Y. Kikuchi, K. Neichi, and A. Yamaguchi. Measurements of induced charge profile in rpc with submilli-strips. *IEEE Transactions on Nuclear Science*, 57(4):2210–2214, 2010.
 - [17] Lorenzo Bonechi, Raffaello D’Alessandro, and Andrea Giannanco. Atmospheric muons as an imaging tool. *Reviews in Physics*, 5:100038, 2020.
 - [18] Antonello Pellecchia. The upgrade of the cms muon system for the high luminosity lhc, 2023.
 - [19] Ahmad Moshaii and Katayoun Doroud. Study the effect of humidity on the rpc performance. *Nuclear Instruments and Methods in Physics Research Section A: Accelerators, Spectrometers, Detectors and Associated Equipment*, 602(3):727–730, 2009. Proceedings of the 9th International Workshop on Resistive Plate Chambers and Related Detectors.

- [20] Christian Lippmann. *Detector Physics of Resistive Plate Chambers*. PhD thesis, Frankfurt U., 2003.
- [21] H. Raether. *Electron Avalanches and Breakdown in Gases*. Butterworths advanced physics series. Butterworths, 1964.
- [22] The ATLAS Collaboration. The atlas experiment at the cern large hadron collider. *Journal of Instrumentation*, 3(08):S08003, aug 2008.
- [23] R. Adolphi et al. The CMS experiment at the CERN LHC. *JINST*, 3:S08004, 2008.
- [24] L.J. Schultz, K.N. Borozdin, J.J. Gomez, G.E. Hogan, J.A. McGill, C.L. Morris, W.C. Priedhorsky, A. Saunders, and M.E. Teasdale. Image reconstruction and material z discrimination via cosmic ray muon radiography. *Nuclear Instruments and Methods in Physics Research Section A: Accelerators, Spectrometers, Detectors and Associated Equipment*, 519(3):687–694, 2004.
- [25] Particle Data Group. Particle data group, 2012. Accessed: November 14th, 2023.
- [26] Rene Brun, Fons Rademakers, Philippe Canal, Axel Naumann, Olivier Couet, Lorenzo Moneta, Vassil Vassilev, Sergey Linev, Danilo Piparo, Gerardo GANIS, Bertrand Bellenot, Enrico Guiraud, Guilherme Amadio, wverkerke, Pere Mato, TimurP, Matevž Tadel, wlav, Enric Tejedor, Jakob Blomer, Andrei Gheata, Stephan Hageboeck, Stefan Roiser, marsupial, Stefan Wunsch, Oksana Shadura, Anirudha Bose, CristinaCristescu, Xavier Valls, and Raphael Isemann. root-project/root: v6.18/02, June 2020.
- [27] L Bonechi. *Misure di raggi cosmici a terra con l'esperimento ADAMO*. PhD thesis, University of Florence Florence, Italy, 2004.
- [28] National Institute of Standards and Technology. Security requirements for cryptographic modules. Technical Report Federal Information Processing Standards Publications (FIPS PUBS) 140-2, Change Notice 2 December 03, 2002, U.S. Department of Commerce, Washington, D.C., 2001.
- [29] Ken Mimasu and Verónica Sanz. Alps at colliders, 2014.
- [30] M. P. Balandin, V. M. Grebenyuk, V. G. Zinov, A. D. Konin, and A. N. Ponomarev. Measurement of the lifetime of the positive muon. *Soviet Journal of Experimental and Theoretical Physics*, 40:811, November 1975.
- [31] CMS Collaboration. Measurement of the charge ratio of atmospheric muons with the cms detector. *Physics Letters B*, 692(2):83–104, 2010.
- [32] K. Raveendrababu. *Study of glass resistive plate chambers for the INO-ICAL detector*. PhD thesis, Tata Institute of Fundamental Research, 2016. Accessed: 14th November 2023.
- [33] Abhishek NISER . Muoscope_Project_2024.
https://github.com/abhich2507/Muoscope_Project_2023, 2023. Accessed: April 23, 2024.